Analysis and modelling of wake-airfoil interaction aeroacoustics

Marios I. Spiropoulos, Filipe R. Do Amaral, Florent Margnat, Vincent Valeau, Peter Jordan, Laurent Philippon, Damien Eysseric

Aeroacoustics Conferences
June 4-7, 2024, Rome, Italy
30th AIAA/CEAS Aeroacoustics Conference (2024)

10.2514/6.2024-3055

Analysis and modelling of wake-airfoil interaction aeroacoustics

Marios I. Spiropoulos*, Filipe R. do Amaral †, Florent Margnat ‡, Vincent Valeau §, Peter Jordan ¶, Laurent Philippon ‖, and Damien Eysseric **
Institut Pprime, CNRS - Université de Poitiers - ISAE ENSMA, Poitiers 86000, France

Motivated by the problem of the sound generated by the interaction of a landing-gear wake with a deployed flap, we investigate the flow and sound fields generated by the interaction of a cylinder wake and a downstream airfoil orthogonally aligned with respect to the cylinder. Detailed experiments (stereo-PIV, acoustic measurements) have been conducted in an anechoic wind tunnel and the data post-processed using spectral proper orthogonal decomposition has been applied to develop low-rank representations of the flow field. The low-rank flow data is used to inform semi-empirical source models in the framework of Howe's vortex-sound theory. Sound propagation is modelled using compact Green's functions obtained using the source panel method. Finally, we employ the previous tools to derive a simplified model for the far-field acoustic pressure.

I. Introduction

Noise reduction is becoming more and more vital for the aviation industry, since stricter regulations are being imposed over the years. The ongoing increase of air traffic leads to more frequent community noise exposure, especially in regions close to airports. Airframe noise is considered as one of the major contributors to aircraft noise, especially during the phase of approach. It has been observed that when the high-lift devices are deployed the sound levels induced by the interaction of the landing gear wake with the deployed flap is a major airframe noise component, since it can exceed the landing gear-noise [1]. Experiments have been conducted to investigate the far-field acoustic radiation [2], [1], while flow measurements and numerical simulations have been used to investigate the aerodynamic field in the vicinity of the landing gear and the downstream flap [3]. Means of noise reduction have also been proposed such as the use of porous materials at the leading edge of the flap [4]. However, the mechanism of sound generation due to the interaction of the landing gear wake with the surface of the flap is not fully understood.

We employ theory of vortex sound to provide a simplified model that captures the basic physics of the problem. We consider a simplified configuration of a cylinder and a downstream NACA 0012 airfoil, oriented perpendicularly to each other that represent the landing-gear strut and the flap accordingly. The impinging vortices on the downstream airfoil are represented by a simplified model, informed by the experimental data, and a tailored low frequency Green's function accounts for the acoustic scattering. The remainder of the paper is organised as follows. In Section II an experimental investigation of the simplified configuration is presented. Stereo-Particle Image Velocimetry (PIV) and synchronised acoustic measurements are described, while in Section III we analyse the obtained data (using Spectral Proper Orthogonal Decomposition [5]) and propose a low-order representation of the vorticity field via a semi-empirical, data-informed model. The Green's function is based on the theory of compact Green's functions of Howe [6] and is presented in Section IV. Finally, in the last Section we use Howe's theory of vortex sound to make a prediction for the radiated sound.

II. Experimental procedure

The experiments were performed in Pprime Institute's anechoic wind tunnel BETI. A cylinder of diameter $d = 20$ mm was placed at the exit nozzle of the convergence and a NACA 0012 airfoil, with a chord of $c = 100$ mm and zero angle of incidence further downstream. The flow speed was set at $U = 30$ m/s which corresponds to a Mach number

*PhD Candidate, marios.spiropoulos@univ-poitiers.fr
†Post-Doctoral Research Fellow, Département Fluides, Thermique, Combustion, filipe.ramos.do.amaral@univ-poitiers.fr
‡Assistant Professor, florent.margnat@univ-poitiers.fr
§Professor, vincent.valeau@univ-poitiers.fr
¶Research Director, peter.jordan@univ-poitiers.fr
‖Assistant Engineer,laurent.philippon@univ-poitiers.fr
**Assistant Engineer, damien.eysseric@univ-poitiers.fr

$M = 0.09$ and Reynolds number $Re = 2.02 \times 10^5$ based on the chord of the airfoil. The distance between the leading edge of the NACA 0012 and the cylinder is 10 cylinder diameters ($D/d = 10$). Furthermore, two microphones were placed symmetrically above and below the center of the airfoil at a distance of $6.9c$. A sketch of the experimental setup and the coordinate system is shown in Fig. 1.

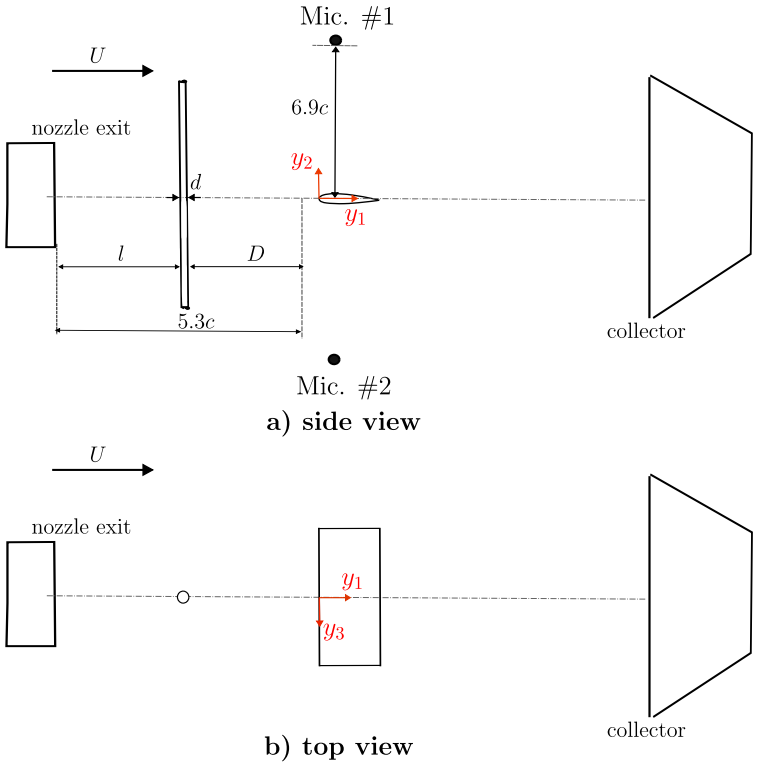

Fig. 1 Sketch of experimental set up and coordinate system with the origin fixed at the leading edge of the NACA 0012 airfoil. The parameters l, D denote the distance between the cylinder and the exit nozzle and the distance between the cylinder and the airfoil respectively.

The three components of the velocity field (u_1-stream-wise, u_2-parallel to the cylinder's span, u_3-parallel to the airfoil's span) around the airfoil were measured using stereoscopic particle image velocimetry. LaVision hardware was used to acquire the measurements, while the velocity field was obtained after post-processing on Davis (LaVision-Software). The time between two laser expositions was 40 μs . Two planes were considered: i) the plane $(y_1 - y_2)$ as shown in Fig. 1a and ii) the plane $(y_1 - y_3)$. The origin of both planes lies at the leading edge and mid-span of the airfoil. For measurements taken in the $(y_1 - y_2)$ plane (Fig. 2a) an acquisition frequency (f_{acq}) of 6 kHz was used while the field of view was 600×200 mm^2, that is $(N_{y_1}, N_{y_2}) = (389, 136)$ grid-points in Cartesian coordinates. For the measurements taken in $(y_1 - y_3)$ (Fig. 2b) the laser sheet lies 3 mm above the leading edge of the airfoil, acquisition frequency was set to 6.25 kHz and the field of view 400×350 mm^2, that is $(N_{y_1}, N_{y_3}) = (286, 266)$ grid-points in Cartesian coordinates. The sampling duration for both experiments was $T_s = 4$s that is $N_t = 24721$ snapshots, for $(y_1 - y_2)$ and $N_t = 24521$ for $(y_1 - y_3)$. Table 1 summarises the basic parameters of the PIV-measurements for each plane. Finally, the microphones and the cameras were synchronised, allowing simultaneous recording of the acoustic and flow-field.

Parameters	Vertical	Horizontal
f_{acq}	6 kHz	6.25 kHz
(N_{y_1}, N_{y_2})	(389, 136)	(286, 266)
Field view	600×200 mm^2	400×350 mm^2
T_s	4 s	4 s
N_t	24721	24521

Table 1 Basic Parameters of the PIV experiment

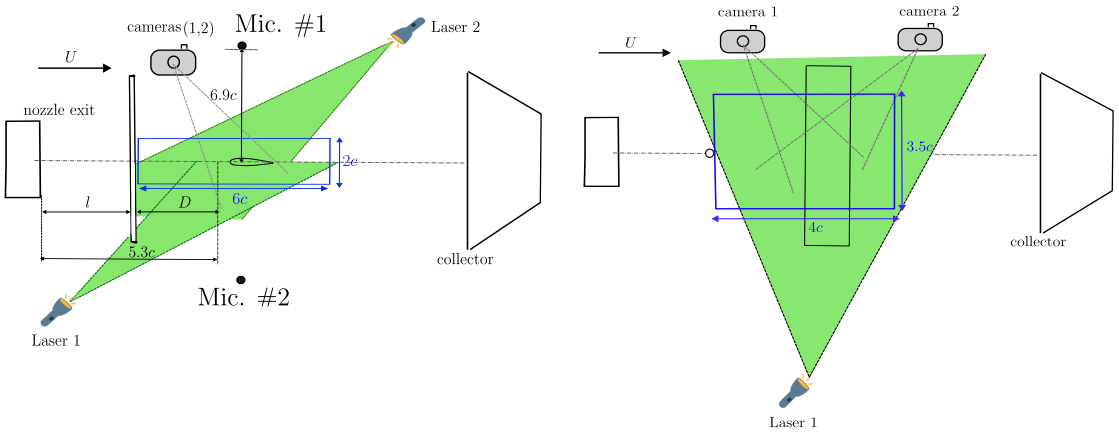

a) Vertical Plane b) Horizontal Plane

Fig. 2 Planes chosen for the stereo-PIV measurements: a) $(y_1 - y_2)$ plane, b) $(y_1 - y_3)$ plane. The PIV-window is indicated by the blue frame in both planes.

III. Link between far field acoustics and flow field around the airfoil

The acoustic measurements reveal that the interaction of the cylinder-wake with the downstream airfoil leads to an increase of Sound Pressure Level (SPL) compared to that obtained when only the cylinder or only the airfoil are present (Fig. 3). Similar results are obtained by the microphone below the airfoil as one might expect on the basis that the sound field should be predominanly driven by a lift dipole perpendicular to the airfoil. The spectra of Fig. 3 are broadband but with a peak close to $St = 0.39$, where the Strouhal number is based on the diameter of the cylinder. Were we considering aeolian tones, such sound generation would be associated with the subdominant drag dipole. We will see later why this frequency dominates the interaction sound.

The instantaneous field of the velocity fluctuations is shown in Figs. 4, 5 for the vertical and the horizontal plane respectively. The vortices in the wake of the cylinder get cut at the leading edge of the airfoil while it is observed that the fluctuation field has a finite support along the span of the airfoil.

The connection between the aerodynamic and acoustic far field can be illustrated by computing the coherence of the velocity signals with those obtained by the acoustic measurements. We use the following definition of the coherence function:

$$\gamma_{xy}(St) = \frac{\left|S_{xy}(St)\right|}{\sqrt{S_{xx}(St)S_{yy}(St)}}, \tag{1}$$

where x, y denote the signals for which the coherence is computed, S_{xy} the cross spectral density between x, y and S_{xx}, S_{yy} the power spectral densities of signals x, y respectively. The cross- and power-spectral densities were obtained by employing Welch's method with $N_{fft} = 256$ number of points in each block, 75% overlap and a Hanning window applied. Figure 6 depicts the coherence plots between the acoustic measurements obtained by the microphone above the airfoil (Mic. #1 in Fig. 1a) and each component of the velocity field, for all grid-points around the airfoil at the peak

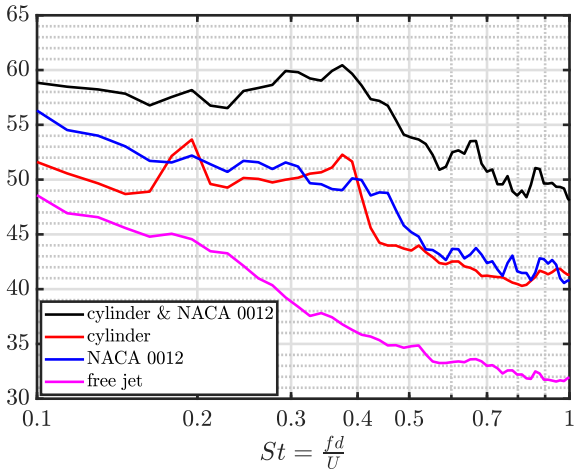

Fig. 3 Sound pressure level (in dB) computed by measurements of the microphone above the center of the NACA 0012 (Mic.1) when i) the cylinder and the airfoil are present, ii) only the cylinder is present, iii) only the airfoil is present and iv) no object lies inside the windtunnel. The reference pressure is $p_{ref} = 2 \times 10^{-5}$ Pa.

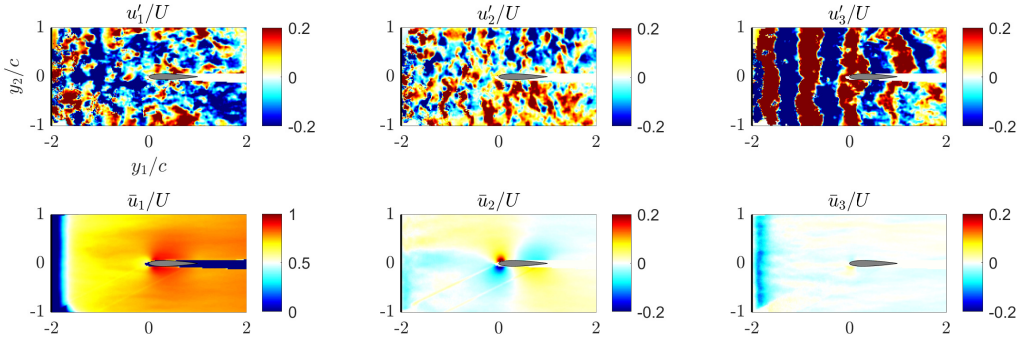

Fig. 4 Velocity components on the $y_1 - y_2$ plane (perpendicular to the airfoil). The top row shows a snapshot of the velocity fluctuation field (u') normalised by the infinite velocity U while the time averaged velocity components ($\bar{u}$) are shown in the bottom row. The cylinder's surface is located at $y_1/c = -2$.

radiation frequency $St = 0.39$. It is observed that the upwash/down-wash (u_2') velocity fluctuation close to the leading edge is strongly correlated with the acoustic field. This is another indicator that the unsteady lift generated at the leading edge is the mechanism associated with sound production when the shed vortices in the wake of the cylinder impinge on the airfoil.

A. SPOD analysis of PIV data

To explore in more detail the source term and the coherent structures from which it is composed we are interested in a low-rank representation of the velocity field around the airfoil. Spectral proper orthogonal decomposition has been employed to decompose the cross-spectral density (CSD) of the velocity components into an orthonormal basis, that optimally represents the data in terms of energy for a given internal product, here defined using the turbulent kinetic energy norm. The SPOD modes are obtained at each frequency as the solution of the following eigenvalue problem:

$$\mathbf{CW\Phi} = \mathbf{\Phi\Lambda}, \tag{2}$$

where $\mathbf{C}$ is the CSD of the velocity field, $\mathbf{W}$ accounts for both the turbulent kinetic energy norm and the numerical quadrature weights, and $\mathbf{\Phi}, \mathbf{\Lambda}$ correspond to the SPOD modes and eigenvalues respectively. The CSD is evaluated by

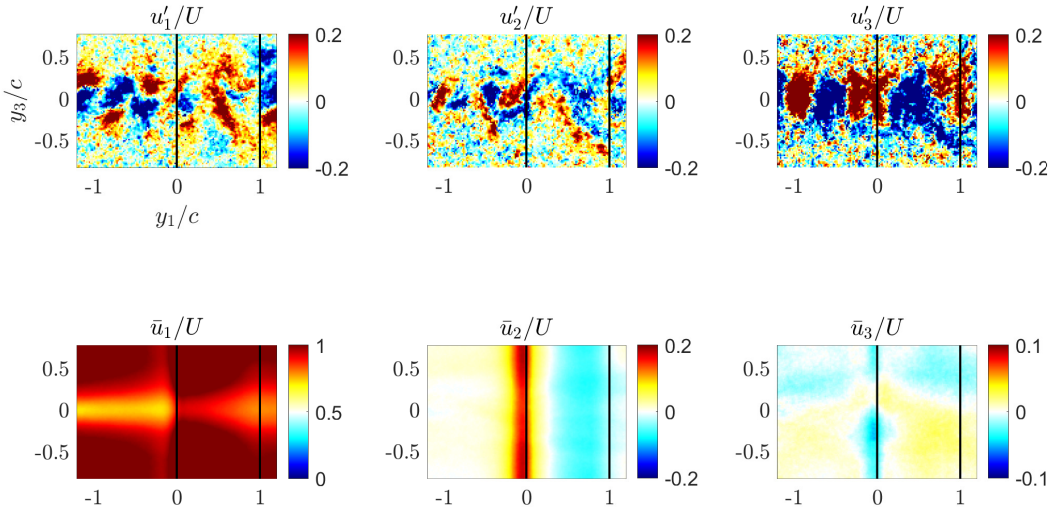

Fig. 5 Velocity components on the $y_1 - y_3$ plane (parallel to the airfoil). The top row shows a snapshot of the velocity fluctuation field (u') normalised by the infinite velocity U while the time averaged velocity components ($\bar{u}$) are shown in the bottom row. The cylinder's surface is located at $\mathbf{y_1/c = -2}$ and the vertical black lines correspond to the leading and trailing edges of the airfoil.

applying the Welch's method, using blocks with $N_{\text{fft}}^{\text{SPOD}} = 128$ size and 50% overlap, providing a total of 386 blocks for the $(y_1 - y_2)$, and 312 blocks for $(y_1 - y_3)$. Furthermore, a hamming tapering window was applied over all blocks to reduce spectral leakage. For more details on the method the reader is referred to [5], [7].

At the radiation peak $St = 0.39$ the eigenvalues are shown in Fig. 7, while Fig. 8 shows the energy accumulated by an ensemble of N_{modes}. The behaviour of the system is high-rank, since there is not an important gain separation between the modes. Taking the first 20 modes we account for about 40% of the turbulent kinetic energy and preserve the coherence between the acoustic field and the flow components.

The low-order representation of the velocity fluctuation field is shown in Fig. 9 for $(y_1 - y_2)$ and in Fig. 10 for $(y_1 - y_3)$. The obtained low rank-velocity field contains the most energetic structures of the flow and it will be used to construct a first order approximation of the flow field.

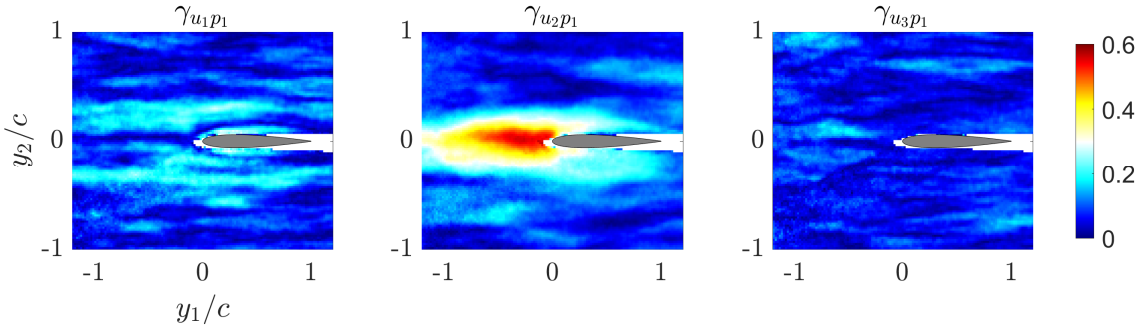

Fig. 6 Coherence between microphone 1 (p_1) and flow measurements, at St = 0.39.

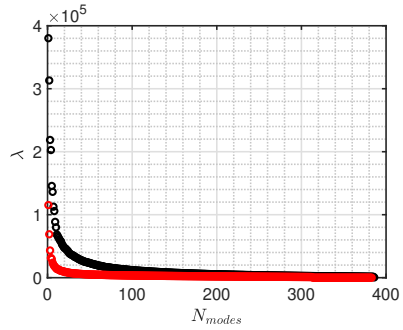

Fig. 7 Eigenvalues of SPOD for the vertical (black) and horizontal (red) planes.

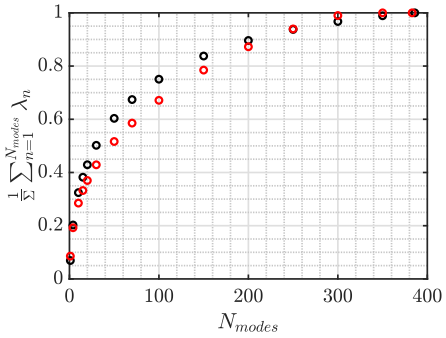

Fig. 8 Amount of energy that an ensemble of N_{modes} accounts for: the black and red dots correspond to the SPOD modes computed for the vertical and horizontal planes respectively. Σ corresponds to the sum of all eigenvalues.

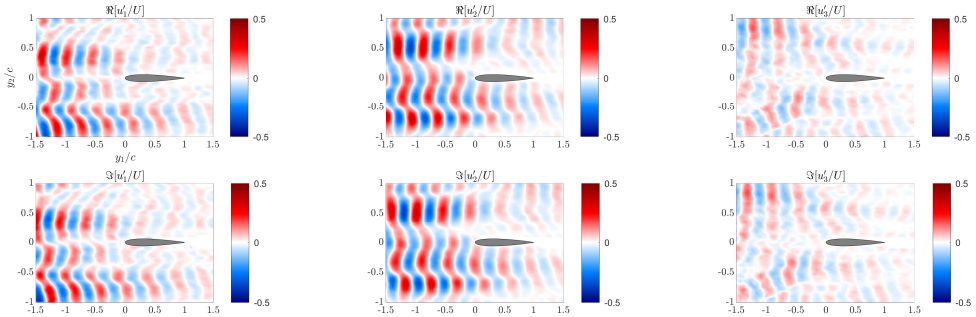

Fig. 9 Reconstructed velocity field by the 20 leading modes, ($y_1 - y_2$) plane at St = 0.39. The top and bottom rows correspond to the real $\Re[\cdot]$ and imaginary $\Im[\cdot]$ parts respectively.

B. Aeroacoustic source-model

For low Mach numbers, the acoustic pressure in the far field is described by Howe's Theory of Vortex Sound [8].

$$p = -\rho \int_V (\vec{\omega} \times \vec{u}) \cdot \vec{\nabla} G dV, \tag{3}$$

where $\vec{\omega} \times \vec{u}$ the Lamb-vector, G the Green function, tailored to the airfoil and V the integration region, defined as the region where $\vec{\omega} \neq 0$ [9]. To first order we may simplify Eq. (3) and express the acoustic dipole that radiates parallel to the lift-direction as follows

$$p_2 = -\rho U \int_V \omega_3 \frac{\partial G}{\partial y_2} dV, \tag{4}$$

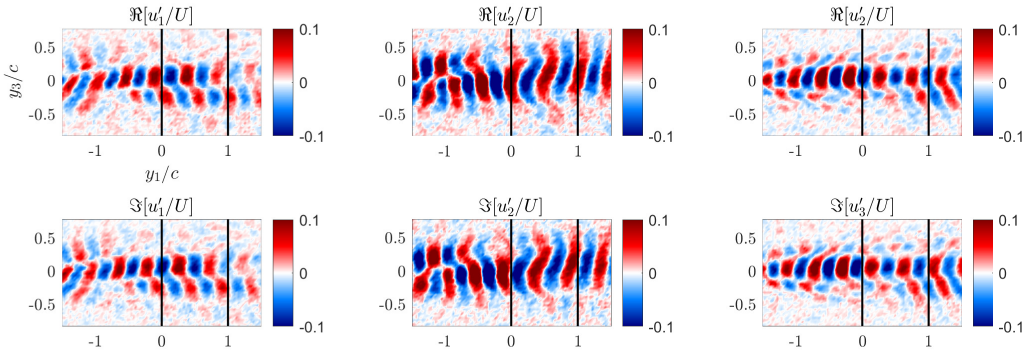

Fig. 10 Reconstructed velocity field by the 20 leading modes, ($y_1 - y_3$) plane St = 0.39. The top and bottom rows correspond to the real $\Re[\cdot]$ and imaginary $\Im[\cdot]$ parts respectively.

The vorticity field of the low-rank model is obtained by computing the curl of velocity field, specifically for ω_3 we have,

$$\omega_3 = \frac{\partial u_1'}{\partial y_2} - \frac{\partial u_2'}{\partial y_1}$$

Using a Richardson's derivation scheme [10] with accuracy of order $O(\Delta x^4)$ we compute the vorticity fluctuation field from the reduced-rank velocity field. The real and imaginary parts of the low-rank representation of the vorticity field is shown in Fig. 11

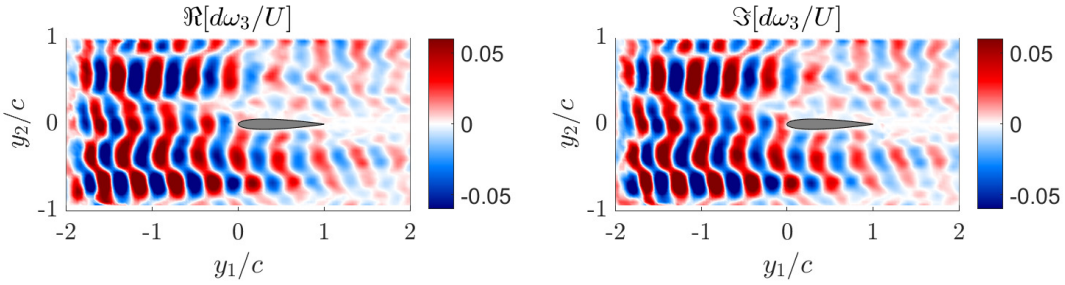

Fig. 11 Real (left) and imaginary (right) part of the vorticity field, obtained by the low rank representation of the velocity field.

It can be seen from Fig. 11 that the vorticity field shows a periodic structure in the y_1-direction which can be described based on the convective wavenumber k_1 defined as

$$k_1 = \frac{2\pi St}{d},$$

which decays as $y_1 \to \infty$. More information about the dependence on the y_2 coordinate is obtained by taking the wave-number transform in the y_2 direction. Hence, we may write

$$\Omega_3(k_2, St, y_1, y_3) = \int_{-\infty}^{\infty} \omega_3(y_1, y_2, y_3, St) e^{ik_2 y_2} dy_2, \tag{5}$$

The transformed vorticity field is plotted at the peak radiation frequency in Fig. 12 as a function of the dimensionless wave-number $k_2 c$ and the coordinate y_1.

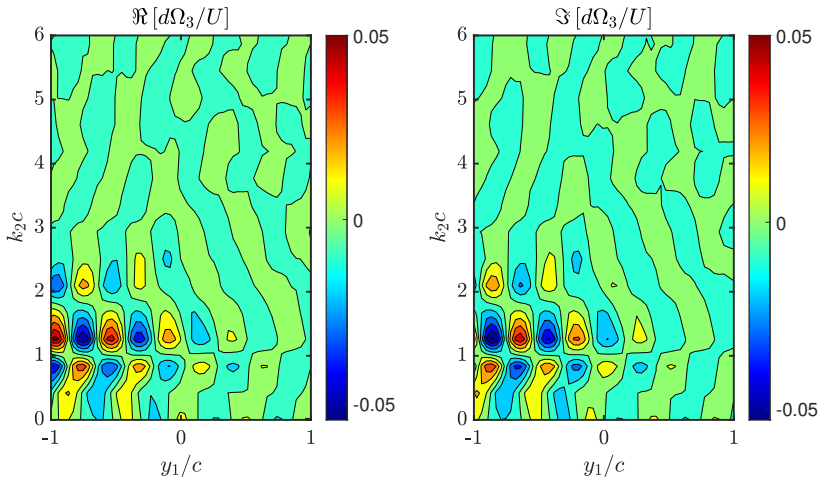

Fig. 12 Wave-number transform of the vorticity field in the y_2 direction.

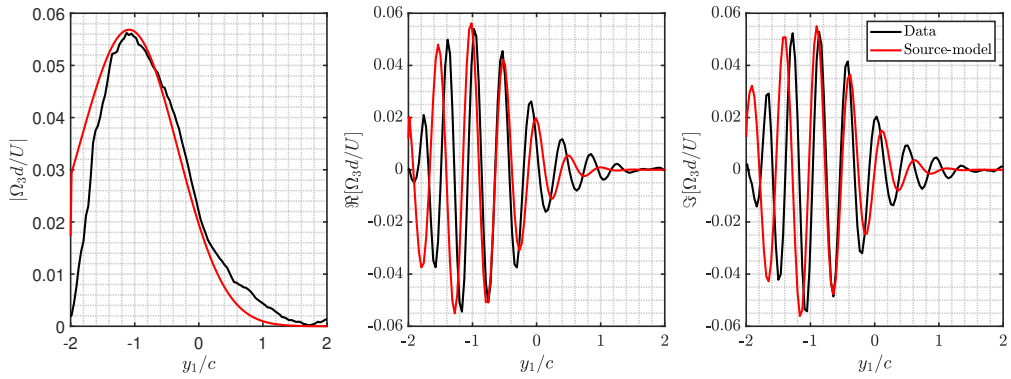

Fig. 13 Comparison of the amplitude (left) and the real (middle) and imaginary (right) part of the semi-empirical model against the low rank representation of the vorticity field, for St = 0.39 and kc = 1.25.

The proposed model to fit the vorticity field close to the leading edge reads as,

$$\Omega_3 = A_0 \exp\left(-\frac{(y_1/c+a)^2}{L_1^2}\right)\left(1-\mathrm{erf}\left(\frac{y_1/c}{L_2}\right)\right)e^{i(k_1c)y_1/c}e^{i(k_2c)y_2/c}S(y_3)H(y_1/c+2), \tag{6}$$

where $H(\cdot)$ the Heaviside step-function, A_0 an amplitude parameter, L_1, L_2, a length scales that will be chosen to fit the data and $S(y_3)$ a function that shows dependence on the distribution of the fluctuation field across the span of the airfoil and k_1, k_2 the wavenumbers in the y_1, y_2 directions. The streamwise wavenumber k_1, is computed for $St = 0.39$ corresponding to the maximum radiation frequency for which we obtain a 60% coherence with the far-field sound. We chose the wavenumber in the y_2 direction with the highest amplitude at $St = 0.39$, that is $k_2c = 1.25$ (see Fig. 12). Therefore, $St = 0.39$ and $k_2c = 1.25$ we choose $A_0 = 0.0344$, $L_1 = 1.2$, $L_2 = 2.5$, $a = 0.9$ to fit the data. A comparison between the proposed source-model and the vorticity fluctuation field of Eq.(5), for $k_2c = 1.25$, $St = 0.39$ and $y_3 = 0$ is shown in Fig. 13.

On the $(y_1 - y_3)$ plane it is not possible to compute the vorticity field (ω_3) from the data, since information regarding the distribution of u_1' as a function of y_2 is missing. Therefore, the dependence of the fluctuation field on the span-direction of the airfoil via the function $S(y_3)$ can be obtained by observing the low order reconstructed velocity field on that plane. The upwash/downwash velocity fluctuation (u_2') close to the leading edge is considered, since it is the one that correlates the most with the far-field microphones (see Fig. 6). It can be described by a Gaussian distribution around the midspan as

$$S_{u_2'}(y_3) = A_{L_3} e^{-\left(\frac{y_3/c}{L_3}\right)^2}, \tag{7}$$

where $A_{L_3} = 0.16$ and $L_3 = 2d/c$ the amplitude and the support of the upwash/downwash velocity fluctuation (u_2') after the vortex is cut by the leading edge. The comparison between Eq. (8) and the data is shown in Fig. 14. The non-dimensional amplitude parameter A_{L_3} is associated to the velocity fluctuation field, therefore it will not be included in Eq. (6). The y_3-dependence of the fluctuation field and the extent of the wetted region across the airfoil span (L_3) is considered, hence we write

$$S(y_3) = S_{u_2'}(y_3)/A_{L_3} \tag{8}$$

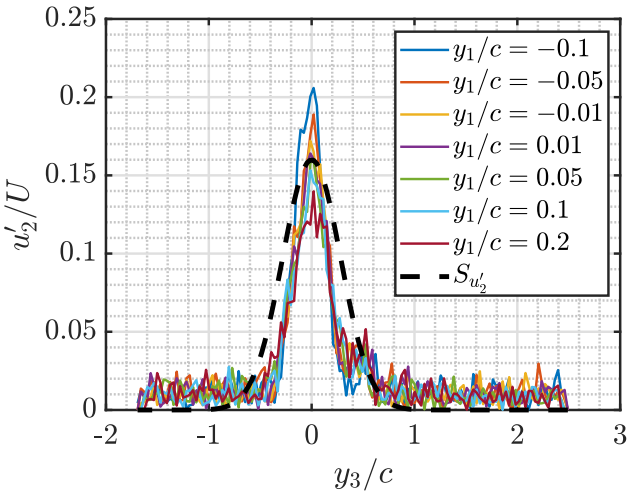

Fig. 14 Comparison of the amplitude of the velocity fluctuation field u_2' with the proposed source-model. The velocity field is normalized by U.

IV. Low frequency Green's function

The source model of the previous section [Eqs. (6), (8)] will be used here to compute the sound radiation. We treat the problem of acoustic scattering of the sound source around a rigid body with an infinite span. The experimental results (Section II) and the analysis shown in Section III indicate that most of the noise emission is observed in a frequency band $St \in [0.19, 0.59]$ with a peak at the double of the vortex shedding frequency $St = 0.39$. This corresponds to acoustic wavelengths $k = \frac{2\pi St}{d} M$ and hence for an airfoil of chord $c = 100$ mm, the Helmholtz number range is given as

$$He = kc = [0.54, 1.67],$$

which leads to the conclusion that the acoustic scattering happens in the low-frequency regime, therefore we are permitted to use low frequency approximations such as the theory of compact Green's functions [8], [6]. In the remainder of the paper the letter x will correspond to the position of the far-field observer while y to the source location.

The compact Green function is a low-frequency approximation of the exact solution of the Helmholtz equation with appropriate boundary conditions that describes the scattering of a wave impinging on an obstacle of arbitrary geometry. In the low-frequency regime, Howe has shown that the Green function can be calculated by using the reciprocal theorem as [6]

$$G(\vec{y}, \vec{x}, \omega) = -\frac{e^{ik|\vec{X}-\vec{Y}|}}{4\pi|\vec{X}-\vec{Y}|}. \tag{9}$$

The Kirchhoff vectors,

$$\vec{X} = \vec{x} - \phi^*(\vec{x}),$$
$$\vec{Y} = \vec{y} - \phi^*(\vec{y}),$$

correspond to the position of the receiver and source corrected by a potential field $\phi^*(\vec{x}), \phi^*(\vec{y})$ that accounts for the distortion of the flow field due to the existence of a rigid obstacle. It is noted that $\phi^*(\cdot) \approx l$, where l the principal dimension of the object immersed in the flow [6]. If we set $\phi^*(\cdot) = 0$ we retrieve the free-field Green function. In other

words, $\phi^*(\cdot)$ accounts for a correction of the free-field Green function to the first order (kl) due to the existence of the object inside the flow region. The Kirchhoff vectors are defined as the velocity potential of a uniform flow with unit velocity in the j-th direction and can be obtained by solution of the Laplace equation (for more details the reader is referred to [6]).

$$\begin{aligned} \nabla^2 Y_j &= 0 \\ \frac{\partial Y_j}{\partial y_n} &= 0 \\ Y_j &\sim y_j \quad \text{as} \quad |y| \to \infty \end{aligned} \tag{10}$$

where $\frac{\partial Y_j}{\partial y_n}$ denotes the normal derivative on the boundary.

For an observer in the far field we may write $\vec{X} \approx \vec{x}$ and then we introduce the following approximations ([6]):

$$\begin{aligned} |\vec{X} - \vec{Y}| &\approx |\vec{x}| - \frac{\vec{x} \cdot \vec{Y}}{|\vec{x}|}, \\ \frac{1}{|\vec{X} - \vec{Y}|} &\approx \frac{1}{|\vec{x}|}. \end{aligned} \tag{11}$$

As a result, Equation (9) reads

$$G\left(\vec{y}, \vec{x}, \omega\right) = -\frac{e^{ik|\vec{x}|} e^{-ik\frac{\vec{x}\cdot\vec{Y}}{|\vec{x}|}}}{4\pi|\vec{x}|}. \tag{12}$$

Furthermore, we write

$$\frac{\vec{x} \cdot \vec{Y}}{|\vec{x}|} = Y_j \cos(\theta_j),$$

where $\theta_j = \cos^{-1}\left[\frac{x_j}{|\vec{x}|}\right]$. The exponential can be written as a sum of Bessel functions using the Jacobi-Anger expansion formula [11] :

$$e^{i(-kY_j)\cos(\theta_j)} = J_0\left(-kY_j\right) + 2\sum_{n\geq 1} i^n J_n\left(-kY_j\right)\cos\left(n\theta_j\right). \tag{13}$$

where i the imaginary unit.

Hence, the Green function and its first spatial derivative in the direction μ are given as,

$$\begin{aligned} G^*\left(\vec{y}, \vec{x}, \omega\right) &= \frac{-e^{ik|\vec{x}|}}{4\pi|\vec{x}|} g_1^* g_2^* g_3^*, \\ \frac{\partial G}{\partial y_\mu}^*\left(\vec{y}, \vec{x}, \omega\right) &= \frac{-e^{ik|\vec{x}|}}{4\pi|\vec{x}|}\left(\frac{\partial g_1^*}{\partial y_\mu} g_2^* g_3^* + g_1^* \frac{\partial g_2^*}{\partial y_\mu} g_3^* + g_1^* g_2^* \frac{\partial g_3^*}{\partial y_\mu}\right), \end{aligned} \tag{14}$$

where,

$$g_j^* = J_0\left(-kY_j\right) + 2\sum_{n\geq 1} i^n J_n\left(-kY_j\right)\cos\left(n\theta_j\right). \tag{15}$$

Further simplifications are introduced and the developements are shown in detail in Appendix A. The final form for the spatial derivative of G^* in the direction μ is the following:

$$\begin{aligned} \frac{\partial G}{\partial y_\mu}^*\left(\vec{y}, \vec{x}, \omega\right) = \frac{k e^{ik|\vec{x}|}}{4\pi|\vec{x}|}\Bigg[& \frac{\partial Y_1}{\partial y_\mu} J_0\left(-kY_2\right) J_0\left(-kY_3\right)\left(-J_1\left(-kY_1\right) + \sum_{n\geq 1} i^n\left(J_{n-1}\left(-kY_1\right) - J_{n+1}\left(-kY_1\right)\right)\cos\left(n\theta_1\right)\right) + \\ & \frac{\partial Y_2}{\partial y_\mu} J_0\left(-kY_1\right) J_0\left(-kY_3\right)\left(-J_1\left(-kY_2\right) + \sum_{n\geq 1} i^n\left(J_{n-1}\left(-kY_2\right) - J_{n+1}\left(-kY_2\right)\right)\cos\left(n\theta_2\right)\right) + \\ & \frac{\partial Y_3}{\partial y_\mu} J_0\left(-kY_1\right) J_0\left(-kY_2\right)\left(-J_1\left(-kY_3\right) + \sum_{n\geq 1} i^n\left(J_{n-1}\left(-kY_3\right) - J_{n+1}\left(-kY_3\right)\right)\cos\left(n\theta_3\right)\right)\Bigg] \end{aligned} \tag{16}$$

Equation (16) provides an approximation for acoustically compact objects, however it is noted that it cannot be used for arbitrarily high frequencies since the Kirchhoff vector correction is valid only to a first-order approximation. As shown in the Appendix, for $kl << 1$ we obtain Howe's compact Green function which reads

$$\frac{\partial G_{kl<<1}}{\partial y_\mu} = -ik\frac{e^{ik|\vec{x}|}}{4\pi|\vec{x}|}\frac{x_j}{|\vec{x}|}\frac{\partial Y_j}{\partial y_\mu}, \tag{17}$$

a summation is intended over j.

A. Region of validity

The proposed approximation is compared against the Green function obtained for a circular cylinder. In this section we will denote the diameter of the cylinder as a, since it is only used to vaidate the proposed Green function and is not related to the experiments described previously. Chaillat et al. obtained the far-field expression for the Green function by applying the method of stationary phase [12] as,

$$G_e\left(\vec{x};\vec{y},\omega\right) = \sum_{n=0}^{\infty}\epsilon_n G_n\left(\vec{x};\vec{y},\omega\right)\cos\left[n\left(\theta-\theta_0\right)\right], \tag{18}$$

where $\epsilon_1 = 1$ and $\epsilon_{n\geq 2} = 2$ and (θ, θ_0) the observer's and source's angular location respectively. Furthermore G_n is given as

$$G_n\left(\vec{x};\vec{y},\omega\right) = \frac{e^{ik\vec{x}|}}{4\pi|\vec{x}|}\left(J_n\left(kr_0\right) - \frac{J_n'\left(ka\right)}{H_n'\left(ka\right)}H_n\left(kr_0\right)\right),$$

(r_0, θ_0), (r, θ) the positions of the source and the far-field observer in polar coordinates. The infinite series of Eq. (18) is truncated and the first N terms are kept. A convergence test for a source close to the cylinder $(y_1, y_2) = (d, d)$ has shown that the series converges at $N = 40$ for Helmholtz numbers $ka \leq 20$. In the following comparisons the first 65 terms of Eq.(18) are kept. Furthermore, Howe's model for the compact Green function and the truncated approximate solution (G^*) shown in Eqs (14), (15) are compared against the truncated exact far-field solution. The Kirchhoff vector is given by Howe [6] as:

$$\begin{aligned} Y_1 &= y_1\left(1+\frac{a^2}{y_1^2+y_2^2}\right), \\ Y_2 &= y_2\left(1+\frac{a^2}{y_1^2+y_2^2}\right), \\ Y_3 &= 0. \end{aligned} \tag{19}$$

The following metric in dB,

$$e = 20\log_{10}\left|\frac{G_e}{G}\right|,$$

is used to illustrate the agreement between the approximate Green functions and Eq. (18).

The error depends on the position of the source around the cylinder, thus the accuracy of the two models is investigated by creating an error map of different source positions around the cylinder at different Helmholtz numbers. The error map is shown in Fig.15. The regions with an absolute logarithmic error between -5 and 5 dB are marked with white colour, while the black regions correspond to errors larger than 5dB. It can be observed that the proposed approximation G^* truncated at the first $N = 100$ terms is more accurate than Howe's compact Green function up to $ka \approx 2$.

B. Source panel-method as a tool to compute low frequency Green's functions

The Kirchhoff vectors can be obtained by solving Eq. (10). Analytical solutions exist for simple shapes such as spheres, cylinders, rigid strips, semi-infinite half-planes or wedges and others [9], [6]. However, taking into account the actual geometry of an airfoil or a more complicated shape requires numerical solutions of Eq. (10) or other techniques based on complex analysis. For instance, Crowdy developed a methodology to calculate the potential flow around multiple rigid objects immersed in a flow [13] which later was applied by Baddoo and Ayton [14] to demonstrate the way that compact Green's functions can be constructed by applying this methodology. Other studies use a numerical

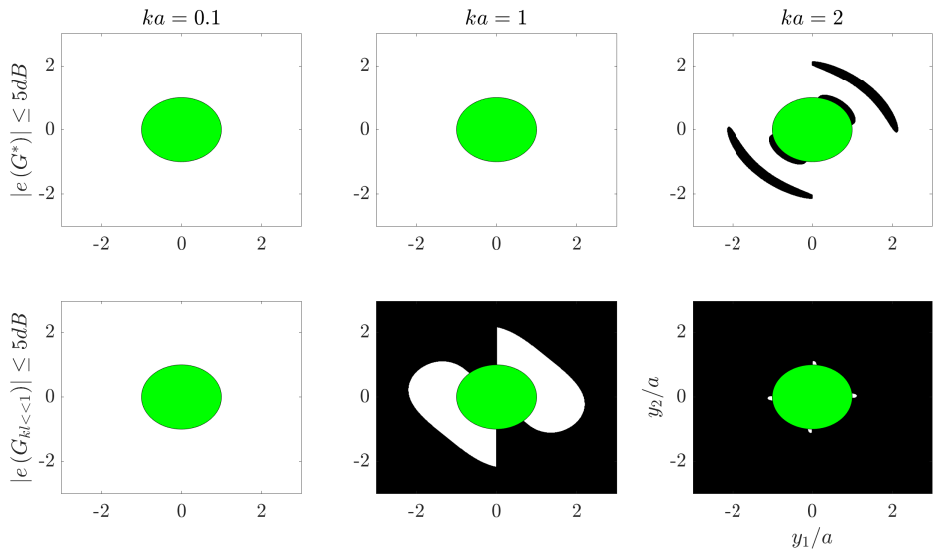

Fig. 15 Error map of the approximations G^* and $G_{kl<<1}$ for different source positions around the object and a fixed observer at $(x_1, x_2) = (10a, 10a)$. White regions corresponds to a logarithmic error $e \in [-5, 5]$(dB) while the darker regions correspond to errors > 5dB. The first row shows the results for $G^*(N = 100)$ while the second row shows the results for Howe's compact Green's function [Eq. (17)].

implementation of the Schwartz-Christoffel mapping, to obtain the Kirchhoff vector by transforming the physical space into the complex plane, solving the potential flow equation and then returning to the physical space [15].

However, in the present work we are interested in modelling finite two-dimensional shapes since for problems with an infinite extent in a homogeneous span-wise direction we may write $Y_3 \approx y_3$. A simple and efficient way to obtain numerical solutions of Eq. (10) is to employ the source panel-method [16], [17]. The surface of the body is divided into panel segments with a corresponding distribution of sources and the uniform flow is parallel to the y_1 or y_2 axis. The numerical implementation of the panel method code is adapted from the book of Fletcher (p.130-136) [17]. As a result, the Kirchhoff vector components Y_j are computed by introducing a free-field velocity $U_j = 1$ in the j-th direction [6].

An illustration is shown for a NACA 0012 airfoil with an angle of incidence $\alpha = 0, 10°$, chord $c = 0.1m$ while the observer is fixed at $\vec{x}_0 = (0, -10c, 0)$ and the location of the source varies on a square grid around the airfoil in a range of $-5 \leq y_1/c \leq 5$ and $-5 \leq y_2/c \leq 5$. Figure 16 depicts the real part of the Green function and its first spatial derivatives. As expected, for the dipolar terms $\left(\frac{\partial G^*}{\partial y_1}, \frac{\partial G^*}{\partial y_2}\right)$ the sources located closer to the edges of the airfoil are more acoustically efficient.

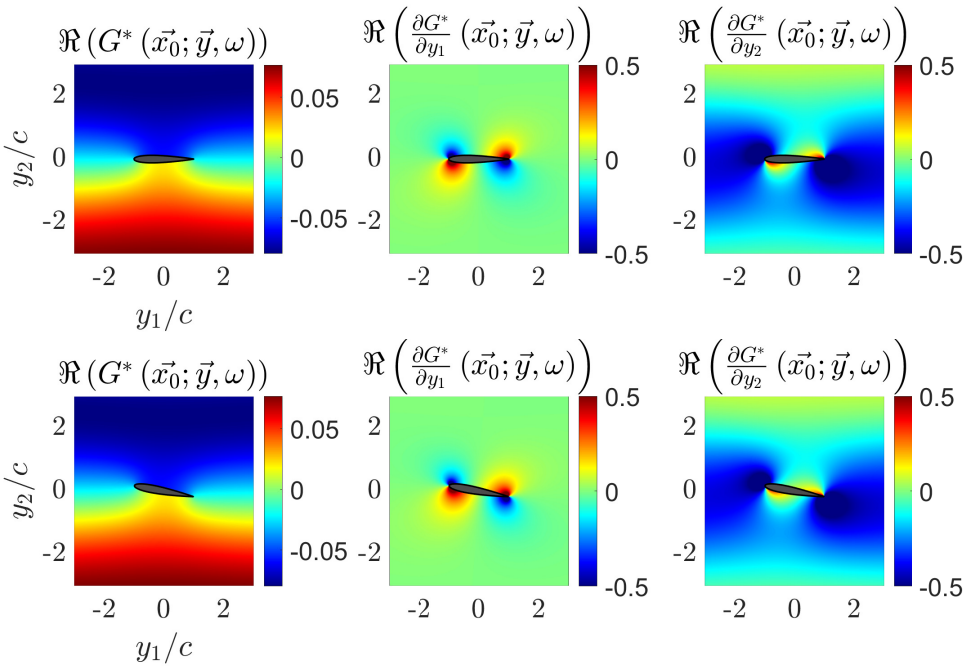

Fig. 16 Proposed approximation for the compact Green function and its first derivatives at kc = 0.5 for an airfoil with chord c = 100 mm at two angles of attack: $\alpha = 0°$ (top), $\alpha = 10°$ (bottom). The observer lies at $\mathbf{x_0}$.

In the next section we will employ the proposed Green function for an airfoil at zero incidence angle to derive a simplified aeroacoustic sound-radiation model.

V. Modelling sound radiation

The final stage of this work is to combine the results of Sections III, IV, and propose a simplified model that will allows us to investigate the physical problem. For the radiation frequency peak $St = 0.39$ the Helmholtz number is $He \approx kY_j \approx 1$ and therefore, we truncate the series and keep only the terms for $n = 1$. The Kirchhoff vector in the spanwise direction of the airfoil reads

$$Y_3 = y_3$$

and hence Eq. (4) becomes

$$\frac{\partial G}{\partial y_2}^* \left(\vec{y},\vec{x},\omega\right) = J_0\left(-ky_3\right)\frac{ke^{ik|\vec{x}|}}{4\pi|\vec{x}|}\mathcal{J}, \tag{20}$$

where

$$\mathcal{J} = \left[\frac{\partial \tilde{Y}_1}{\partial \tilde{y}_2}J_0\left(-kc\tilde{Y}_2\right)\left[-J_1\left(-kc\tilde{Y}_1\right)+i\left(J_0\left(-kc\tilde{Y}_1\right)-J_2\left(-kc\tilde{Y}_1\right)\right)\cos\left(\theta_1\right)\right]+\right. \tag{21}$$

$$\left.\frac{\partial \tilde{Y}_2}{\partial \tilde{y}_2}J_0\left(-kc\tilde{Y}_1\right)\left[-J_1\left(-kc\tilde{Y}_2\right)+i\left(J_0\left(-kc\tilde{Y}_2\right)-J_2\left(-kc\tilde{Y}_2\right)\right)\cos\left(\theta_2\right)\right]\right],$$

where $\tilde{y_j}, \tilde{Y_j}$ denote the source position and Kirchhoff vector non-dimensionalised by the chord length (c).

A. Aeroacoustic model

After considering a Gaussian distribution in the y_3-direction, the expression for the far-field acoustic pressure reads (full derivation shown in Appendices A, B):

$$p = -A\frac{e^{ik|\vec{x}|}\rho U^2}{2\sqrt{\pi}}\frac{c}{|\vec{x}|}\frac{c}{d}\exp\left(-\frac{k^2L_3^2}{8}\right)M_{0,0}\left(\frac{k^2L_3^2}{4}\right)\iint_{-\infty}^{\infty}\tilde{\omega}_3\left(\tilde{y}_1,\tilde{y}_2\right)\mathcal{J}d\tilde{y}_1d\tilde{y}_2, \tag{22}$$

where $\tilde{\omega}_3 = d\omega_3/U$ the non-dimensional vorticity fluctuation in the mid-span at $St = 0.39$ and $M_{\frac{1}{2}\mu,\frac{1}{2}\nu}(\cdot)$ the Whittaker function (for details see [18] p505).

The 20 SPOD modes-reconstructed vorticity field is used as the source term. To taper the fluctuations at the borders of the domain we consider two Gaussians as window functions in the y_1, y_2 directions. The aeroacoustic integral reads then as,

$$p_{\tilde{\omega}_3^{(\mathrm{SPOD})}} = -\frac{e^{ik|\vec{x}|}\rho U^2}{2\sqrt{\pi}}\frac{c}{|\vec{x}|}\frac{c}{d}\exp\left(-\frac{k^2L_3^2}{8}\right)M_{0,0}\left(\frac{k^2L_3^2}{4}\right)\iint_{-\infty}^{\infty}\tilde{\omega}_3^{(\mathrm{SPOD})}\exp\left(-\frac{\tilde{y}_1^2}{L_{G_1}^2}\right)\exp\left(-\frac{\tilde{y}_2^2}{L_{G_2}^2}\right)\mathcal{J}d\tilde{y}_1d\tilde{y}_2. \tag{23}$$

We choose $L_{G_1} = 2$ and $L_{G_2} = 0.6$ so that the tapering-window is an ellipsoid that covers the source region which is defined as the region showing a coherence $\gamma > 30\%$ (Fig. 6). The integration in the $y_1 - y_2$ plane is performed along the PIV field view. The validity of the proposed acoustic model is assessed by comparing the computed SPL in the far field to microphone measurements. An arc of 15 microphones was placed below the airfoil which corresponds to a circular sector with center the center of the airfoil, radius $R = 10c$ and angle $\Theta = 70°$. The arc of microphones with respect to the leading edge corresponds to a circular sector with center the leading edge, $R' \approx 10c$ and an angle of $\Theta' = 103°$ as shown in the sketch of Fig. 17.

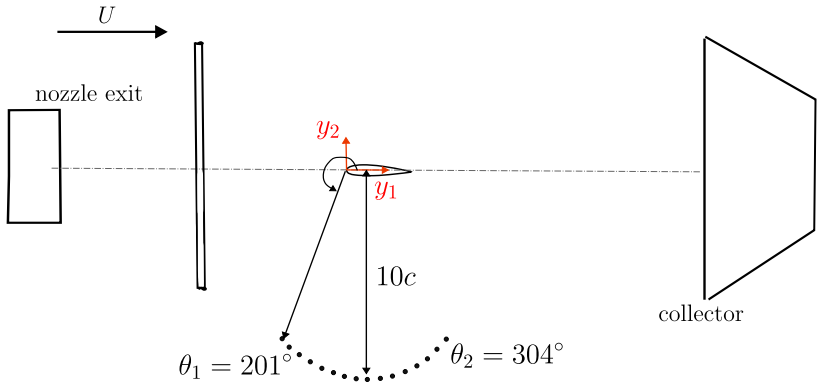

Fig. 17 Microphone arc, placed below the airfoil. The angular locations θ_1 and θ_2 correspond to the first and last microphone of the arc with respect to the leading edge.

The proposed model that describes the vorticity fluctuation-field close to the leading edge with the highest amplitude is obtained by combining Eqs. (6), (8). It follows

$$\Omega_3 = A_0\exp\left(-\frac{(y_1/c+a)^2}{L_1^2} - \left(\frac{y_3}{L_3}\right)^2\right)\left(1-\mathrm{erf}\left(\frac{y_1/c}{L_2}\right)\right)e^{i(k_1y_1+k_2y_2)}, \tag{24}$$

The dependence on y_3 is included in Equation (23) taking advantage the homogeneity of the Green function along the span of the airfoil. The double integral is evaluated numerically as described before with the same tapering-window. Before comparing the far-field spectra a qualitative comparison between the semi-empirical and the SPOD-informed sound radiation model is presented by plotting the integrands of the two aeroacoustic integrals in Fig. 18. The semi-empirical model contains only the most energetic cylinder-span wavenumber, while in the truncated-SPOD field we can observe multiple k_2-modes that interact with each other. Directivity plots of the far-field SPL computed by the acoustic measurements, the semi-empirical and SPOD-informed sound radiation model is shown in Fig. 19.

The following can be concluded: i) the SPOD-informed sound-radiation model is in agreement with the acoustic measurements which validates the proposed Green-function for $St = 0.39$, ii) the semi-empirical model captures the dipolar nature of the directivity however it differs from the one obtained for the SPOD-informed source-term. The amplitude is also overestimated by approximately 5 dB. The proposed semi-empirical source-model is a fit to the most energetic vorticity k_2- mode and hence, the interference effects by other k_2-wavenumbers are neglected, while it seems that the vorticity fluctuations described by the model are strong close to the leading edge, while it does not account for the fluctuations close to the trailing edge.

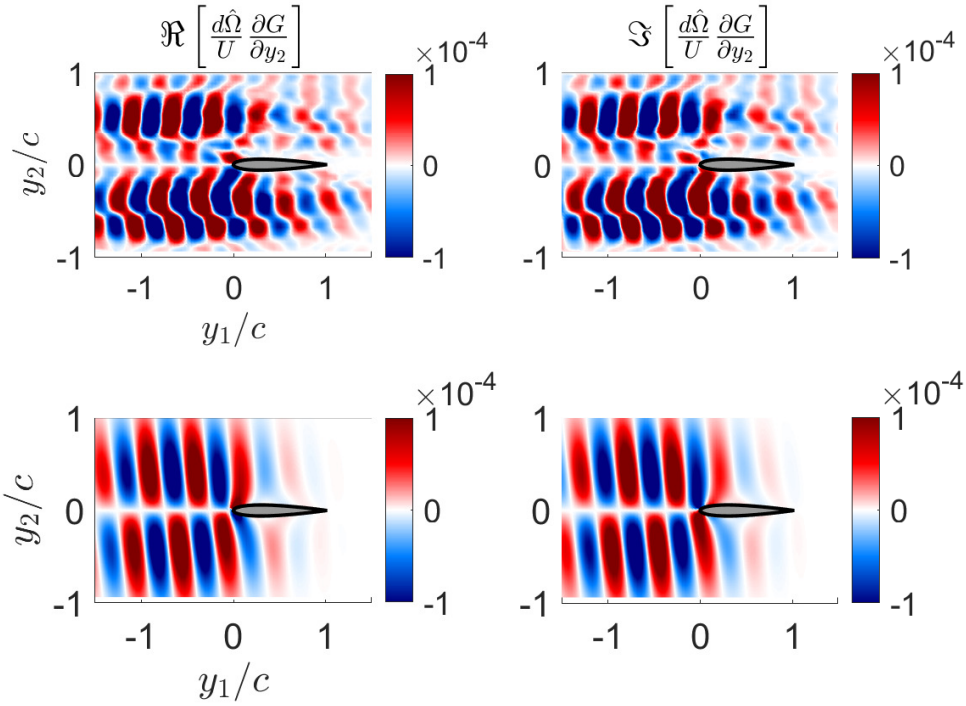

Fig. 18 Integrands of the aeroacoustic integrals for SPOD-informed source term ($\omega_3^{(SPOD)}$) (top row) and semi-empirical model (Ω_3) (bottom row).

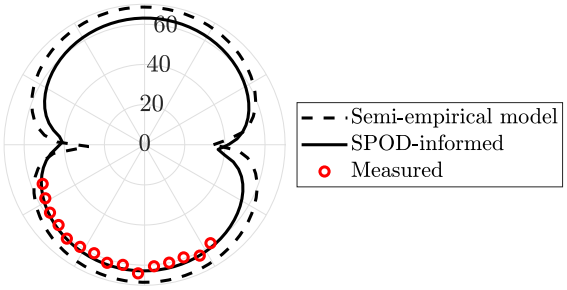

Fig. 19 Directivity plot of the computed sound pressure level at a radial distance $|\mathbf{x}|/c = 10$ for $k_1 c = 2\pi \mathrm{St} c/d$, $k_2 c = 1.25$ and $\mathrm{St} = 0.39$, with reference pressure $p_{ref} = 2 \times 10^{-5}$ Pa.

In the following, we refine the proposed source-model by considering the wave-forms of other k_2-modes. Then, the refined semi-empirical model is constructed by the sum of multiple waveforms used to fit the k_2-modes extracted from the data as

$$\hat{\Omega}_3 = \sum_m \Omega_3^m e^{ik_1 c\tilde{y}_1}, \tag{25}$$

where

$$\Omega_3^m = \bar{A}_m \mathcal{E}_m(y_1) e^{k_2^{(m)} c\tilde{y}_2}, \tag{26}$$

m the summation index, $\bar{A}_m$ the amplitude of each $k_2^{(m)}$-mode and $\mathcal{E}_m(y_1)$ the wave-envelope of each mode that depends on the streamwise direction. The first 8 k_2-modes, that is $k_2 c \in [0, 2.9]$ are plotted on Fig. 20.

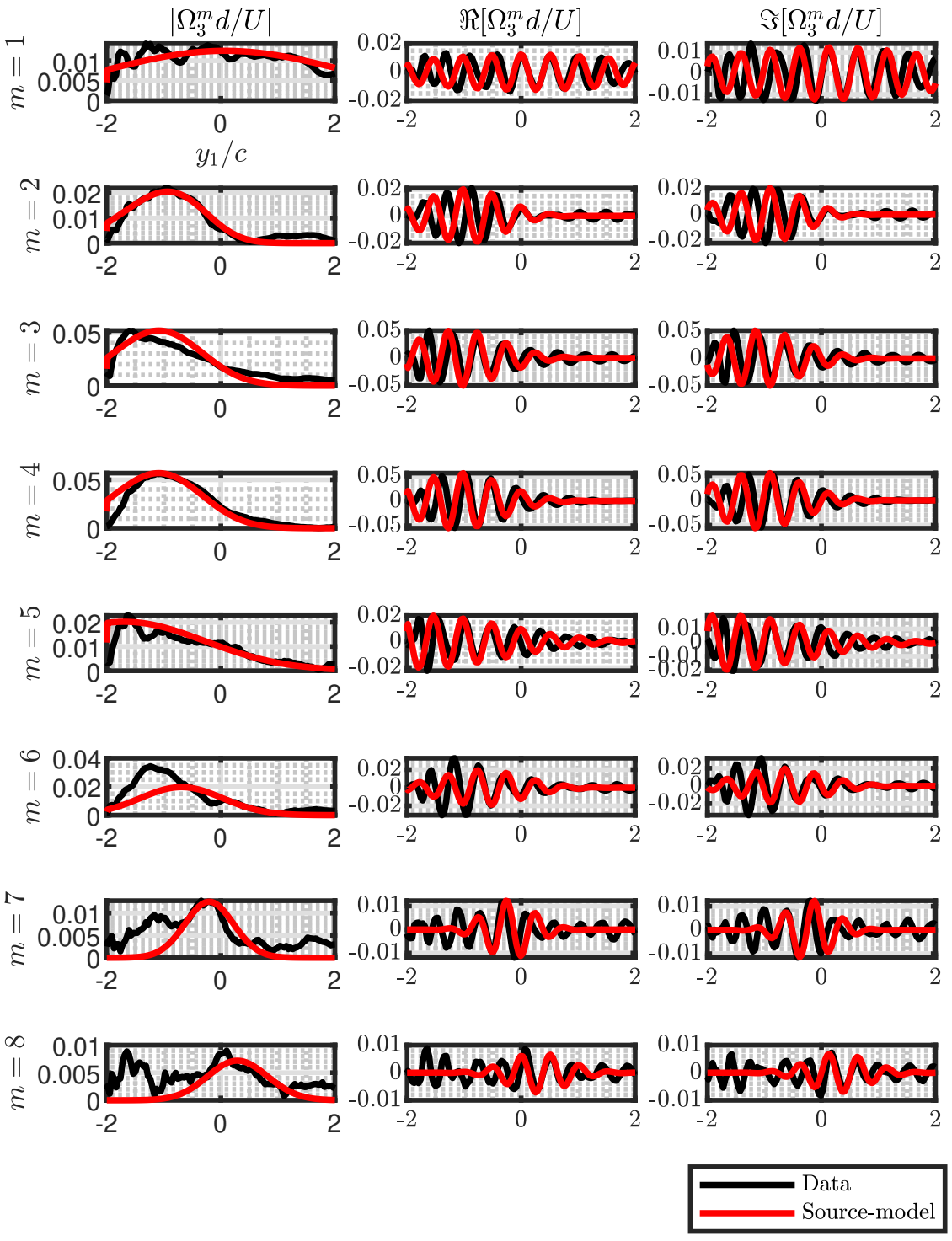

Fig. 20 Fit of the m = 8 first k_2−modes. The solid black line corresponds to the Fourier-transformed SPOD-truncated field and the solid red-line corresponds to the proposed fit.

The fitting of the vorticity field close to the leading edge was achieved by varying the parameters of Eq.(24): a, L_1, L_2 to obtain $\mathcal{E}(y_1)$ and A_0 to obtain $\bar{A}$ for each m. The expression of Eq. (26) is inputted in the aeroacoustic integral and the integrand is shown on Fig. 21 while the comparison between the semi-empirical models [Eqs.(24), (26)], the SPOD-informed source model and the microphones measurements is shown in Fig. 22. Higher k_2-modes increase the vorticity fluctuations at the trailing edge which leads to changes of the sound-field directivity. In terms of amplitude the semi-empirical models overestimate the sound field, however by accounting for more modes the error between the model and measurements is slightly decreased. It can be seen that for higher modes the fitting of the

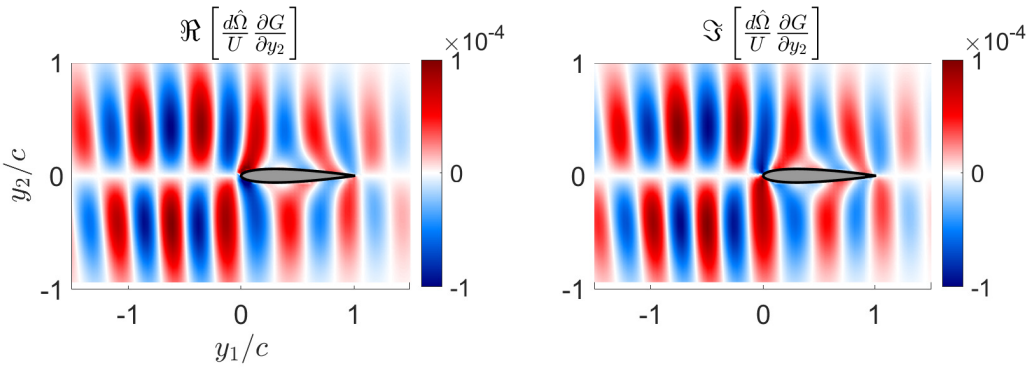

Fig. 21 Integrand of the aeroacoustic integral when 8 k_2−modes are considered [Eq.(26)].

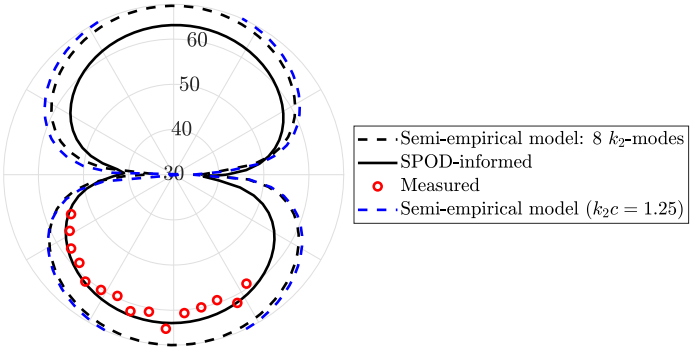

Fig. 22 Directivity plots of the sound filed obtained by a) the semi-empirical model using sum of the first 8 k_2−modes, b) the SPOD-informed acoustic radiation model, c) the measurements obtained by the arc of microphones and iv) the semi-empirical model using the most energetic k_2−mode .

k_2−modes computed from the data with Eq.(24) becomes less accurate upstream of the airfoil. This introduces further errors and therefore influences the directivity and interference effects between the k_2−modes.

B. Acoustic Efficiency

In the following, we study in more detail the acoustic efficiency of each k_2-wavenumber. We consider the wavenumber-transformed, SPOD-truncated vorticity field (Fig. 12) and we represent each mode as

$$\hat{\omega}_3^m = \mathcal{W}_m(\tilde{y}_1, St)\exp\left(-\tilde{y}_3^2/L_3^2\right)e^{ik_2c\tilde{y}_2}, \tag{27}$$

where $\mathcal{W}_m(\tilde{y}_1, St)$ the waveform for each wavenumber k_2 computed at $St = 0.39$. We compute then

$$\Pi_m = -\frac{e^{ik|\vec{x}|}\rho U^2}{2\sqrt{\pi}}\frac{c}{|\vec{x}|}\frac{c}{d}\exp\left(-\frac{k^2L_3^2}{8}\right)M_{0,0}\left(\frac{k^2L_3^2}{4}\right)\iint_{-\infty}^{\infty}\mathcal{W}_m(\tilde{y}_1, St)e^{ik_2c\tilde{y}_2}\exp\left(-\frac{\tilde{y}_1^2}{L_{G_1}^2}\right)\exp\left(-\frac{\tilde{y}_2^2}{L_{G_2}^2}\right)\mathcal{J}\,d\tilde{y}_1 d\tilde{y}_2, \tag{28}$$

Furthermore, we define the acoustic efficiency as

$$\eta = \int_0^{2\pi} |\Pi_m|^2 \, d\theta.$$

Figure 23 depicts η normalised by its maximum value as a function of the non-dimensional wavenumber $k_2 c$. The wavenumbers $k_2 c = 0.83$ and $k_2 c = 1.25$ are the most efficient in terms of sound radiation, however the interference between other k_2-modes leads to changes in the sound directivity in the far-field. The latter can be seen more clearly

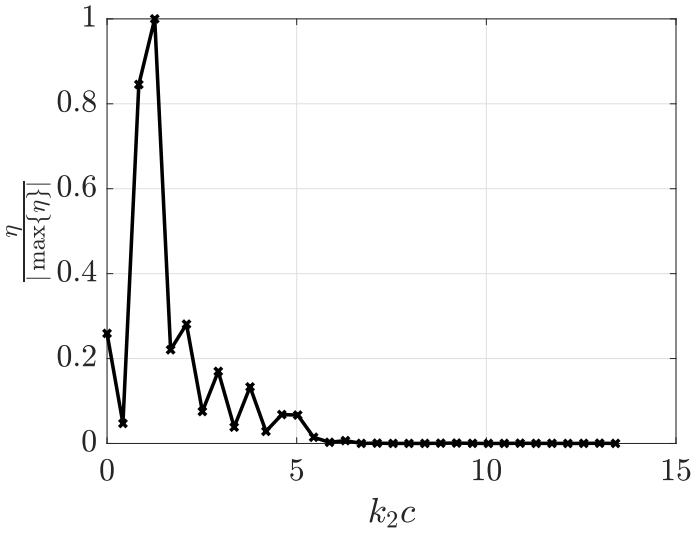

Fig. 23 Acoustic efficiency of k_2-modes.

by investigating the acoustic efficiency of each k_2-mode normalised by its maximum amplitude in Fig. 24. Higher k_2-modes are acoustically efficient despite their low amplitude and thus considering them leads to more accurate description of the sound field. In Figure 25 we plot the estimated far-field SPL when considering the k_2 wavenumbers

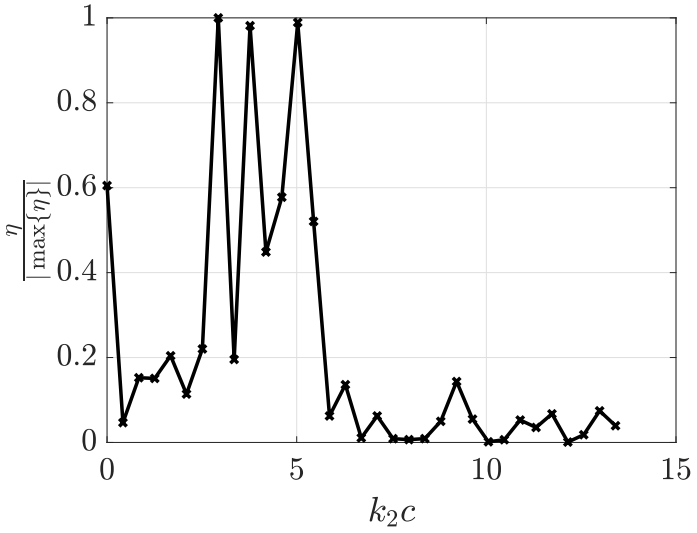

Fig. 24 Acoustic efficiency of k_2-modes normalised by their maximum amplitude.

up to $k_2 c = 5.44$, that is the first 14 vorticity fluctuation k_2-modes as they were obtained by the Fourier transformed 20 SPOD modes-truncated vorticity field. The information contained in the first 14 k_2-modes is enough to describe the source of sound radiation. The semi-empirical model fails to encapsulate the behaviour of the source in the total extent of the source region. Further investigation of the source-term and its link to sound radiation is a subject of future work.

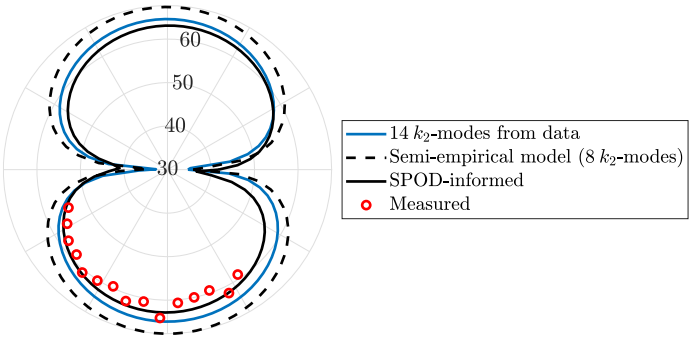

Fig. 25 Comparison of the obtained far-field SPL for different source terms, i) k_2-modes obtained by experiments (blue curve), semi-empirical model fitting the first 8 modes (black dashed curve), truncated 20 SPOD mode representation of the source and the microphone measurements.

Conclusions

We have studied the aeroacoustic problem of a cylinder wake interaction on an airfoil rotated by 90° with respect to the cylinder, so as to mimic the problem of sound generation by a landing gear wake impinging on a deployed flap. An excess in sound pressure field is observed experimentally when both the cylinder and the airfoil are present in agreement with previous works found in literature [1]. Stereo-PIV measurements in two planes, one containing the cylinder axis ($y_1 - y_2$ plane) and the other the airfoil span ($y_1 - y_3$ plane), show that when the shed vortices reach the leading edge of the airfoil, the flow field changes locally and this interaction region is strongly correlated with the measurements obtained by the far-field microphones. SPOD was used to reconstruct a reduced-rank representation of the flow, that conserves the 60% coherence observed with the sound field, and this reduced-rank field is then used to elaborate a semi-empirical model for the source term based on vortex-sound theory.

We have also developed a low-frequency Green function based on Howe's compact Green's functions [6], [9], by using a source panel-method solver for potential flows. Finally, we combine the experimental results, the source model and the low frequency Green's function for the rigid airfoil and compute the far-field sound by using Howe's acoustic analogy. The source term is informed by the truncated SPOD-vorticity field and the computed far-field SPL agrees with the measurements obtained by an arc of microphones. It is concluded that the proposed low-frequency Green function captures the typical dipolar radiation pattern and is in agreement with the experimental observations for $St = 0.39$. A semi-empirical model is derived to model the waveform of the most energetic vorticity mode (Fourier transformed in the k_2-direction). The amplitude of the sound field is overestimated by approximately $5dB$ when the latter is used as source-term. Finally, the semi-empirical model was refined to account for more cylinder-span (k_2) vorticity modes, which leads to better agreement with measurements in terms of amplitude and directivity. However, the fitting of the higher k_2-modes is not accurate upstream the airfoil and thus leads to additional sources of error.

Acknowledgements

This work was supported by the DGAC (Direction Générale de l'Aviation Civile), by the PNRR (Plan National de Relance et de Résilience Français) and by NextGeneration EU via the project MAMBO (Méthodes Avancées pour la Modélisation du Bruit moteur et aviOn.

The authors wish to thank Pascal Biais, Jean-Christophe Vergez and Janick Laumonier for their technical support to this work, and Bouba El Harchi and Vanessa Millet for their administrative support.

References

[1] Oerlemans, S., and Pott-Pollenske, M., "An experimental study of gear wake/flap interaction noise," *10th AIAA/CEAS Aeroacoustics Conference*, 2004, p. 2886.

[2] Pott-Pollenske, M., Almoneit, D., and Saueressig, G., "A Study on Landing Gear Wake-Flap Interaction Noise," *23rd AIAA/CEAS Aeroacoustics Conference*, 2017, p. 3692.

[3] Khorrami, M. R., Mineck, R. E., Fares, E., Yao, C., and Jenkins, L. N., "A comparative study of simulated and measured gear-flap flow interaction," *21st AIAA/CEAS Aeroacoustics Conference*, 2015, p. 2989.

[4] Martinez Lara, F. J., and Angland, D., "The Use of Porous Meshes to Reduce Landing Gear Wake-Flap Interaction Noise," *28th AIAA/CEAS Aeroacoustics 2022 Conference*, 2022, p. 3044.

[5] Towne, A., Schmidt, O. T., and Colonius, T., "Spectral proper orthogonal decomposition and its relationship to dynamic mode decomposition and resolvent analysis," *Journal of Fluid Mechanics*, Vol. 847, 2018, pp. 821–867.

[6] Howe, M. S., *Vortex Sound*, Cambridge Texts in Applied Mathematics, Cambridge University Press, 2002. https://doi.org/10.1017/CBO9780511755491.006.

[7] Schmidt, O. T., and Colonius, T., "Guide to spectral proper orthogonal decomposition," *Aiaa journal*, Vol. 58, No. 3, 2020, pp. 1023–1033.

[8] Howe, M., "Contributions to the theory of aerodynamic sound, with application to excess jet noise and the theory of the flute," *Journal of Fluid Mechanics*, Vol. 71, No. 4, 1975, pp. 625–673.

[9] Howe, M. S., *Acoustics of fluid-structure interactions*, Cambridge university press, 1998.

[10] Koschatzky, V., Westerweel, J., and Boersma, B., "A study on the application of two different acoustic analogies to experimental PIV data," *Physics of Fluids*, Vol. 23, No. 6, 2011.

[11] Cuyt, A. A., Petersen, V., Verdonk, B., Waadeland, H., and Jones, W. B., *Handbook of continued fractions for special functions*, Springer Science & Business Media, 2008.

[12] Chaillat, S., Cotté, B., Mercier, J.-F., Serre, G., and Trafny, N., "Efficient evaluation of three-dimensional Helmholtz Green's functions tailored to arbitrary rigid geometries for flow noise simulations," *Journal of Computational Physics*, Vol. 452, 2022, p. 110915.

[13] Crowdy, D., "A new calculus for two-dimensional vortex dynamics," *Theoretical and Computational Fluid Dynamics*, Vol. 24, 2010, pp. 9–24.

[14] Baddoo, P. J., and Ayton, L. J., "The compact Green's function for multiple bodies," *25th AIAA/CEAS Aeroacoustics Conference*, 2019, p. 2470.

[15] Harwood, A. R., and Dupère, I. D., "Numerical evaluation of the compact acoustic Green's function for scattering problems," *Applied Mathematical Modelling*, Vol. 40, No. 2, 2016, pp. 795–814. https://doi.org/https://doi.org/10.1016/j.apm.2015.10.039, URL https://www.sciencedirect.com/science/article/pii/S0307904X15007015.

[16] Anderson, J., *Fundamentals of Aerodynamics*, McGraw Hill, 2011.

[17] Fletcher, C. A., *Computational techniques for fluid dynamics: Specific techniques for different flow categories*, Springer Science & Business Media, 2012.

[18] Abramowitz, M., and Stegun, I. A., *Handbook of mathematical functions with formulas, graphs, and mathematical tables*, Vol. 55, US Government printing office, 1948.

[19] Gradshteyn, I. S., and Ryzhik, I. M., *Table of integrals, series, and products*, Academic press, 2014.

A. Appendix: Reformulation of acoustically compact Green's function

We start our analysis by expanding the terms g^* of Eq. (15).

$$g_j^* g_k^* = \left[J_0\left(-kY_j\right) + 2\sum_{n\geq 1} i^n J_n\left(-kY_j\right)\cos\left(n\theta_j\right)\right]\left[J_0\left(-kY_k\right) + 2\sum_{n\geq 1} i^n J_n\left(-kY_k\right)\cos\left(n\theta_k\right)\right], \tag{A.1}$$

and expanding the terms

$$\begin{aligned} g_j^* g_k^* = {} & J_0\left(-kY_j\right) J_0\left(-kY_k\right) + 2J_0\left(-kY_j\right)\sum_{n\geq 1} i^n J_n\left(-kY_k\right)\cos\left(n\theta_k\right) + \\ & + 2J_0\left(-kY_k\right)\sum_{n\geq 1} i^n J_n\left(-kY_j\right)\cos\left(n\theta_j\right) + 4\sum_{n\geq 1} i^n J_n\left(-kY_j\right)\cos\left(n\theta_j\right)\sum_{n\geq 1} i^n J_n\left(-kY_k\right)\cos\left(n\theta_k\right), \end{aligned} \tag{A.2}$$

While for the derivatives of g_1^*, g_2^*, g_3^* we may write

$$\frac{\partial g_j^*}{\partial y_i}(\vec{y},\vec{x},\omega) = -k\frac{\partial Y_j}{\partial y_i}\left(\frac{\partial}{\partial(-kY_j)}\{J_0(-kY_j)\} + 2\sum_{n\geq 1} i^n \frac{\partial}{\partial(-kY_j)}\{J_n(-kY_j)\}\cos(n\theta_j)\right)$$
$$= -k\frac{\partial Y_j}{\partial y_i}\left(-J_1(-kY_j) + \sum_{n\geq 1} i^n\left(J_{n-1}(-kY_j) - J_{n+1}(-kY_j)\right)\cos(n\theta_j)\right), \tag{A.3}$$

and the product $\frac{\partial g_j^*}{\partial y_i} g_k^* g_l^*$ is obtained as

$$\frac{\partial g_j^*}{\partial y_i}(\vec{y},\vec{x},\omega) = -k\frac{\partial Y_j}{\partial y_i}\left(-J_1(-kY_j) + \sum_{n\geq 1} i^n\left(J_{n-1}(-kY_j) - J_{n+1}(-kY_j)\right)\cos(n\theta_j)\right)\times$$
$$\left[J_0(-kY_l)\,J_0(-kY_k) + 2J_0(-kY_l)\sum_{n\geq 1} i^n J_n(-kY_k)\cos(n\theta_k) + \right. \tag{A.4}$$
$$\left. +2J_0(-kY_k)\sum_{n\geq 1} i^n J_n(-kY_l)\cos(n\theta_l) + 4\sum_{n\geq 1} i^n J_n(-kY_l)\cos(n\theta_l)\sum_{n\geq 1} i^n J_n(-kY_k)\cos(n\theta_k)\right].$$

As n increases the amplitude of the Bessel function $J_n(z)$ decreases. Provided that Equation (9) works for acoustically compact objects ($kl < 1$) we can simplify Eq. (A.4) by truncating the products of the series as

$$\frac{\partial g_j^*}{\partial y_i} g_k^* g_l^*(\vec{y},\vec{x},\omega) = -kJ_0(-kY_l)\,J_0(-kY_k)\,\frac{\partial Y_j}{\partial y_i}\left(-J_1(-kY_j) + \sum_{n\geq 1} i^n\left(J_{n-1}(-kY_j) - J_{n+1}(-kY_j)\right)\cos(n\theta_j)\right). \tag{A.5}$$

It is further noted that at the limit of very low frequencies $kl << 1$ it can been seen that

$$J_0(-kY_l) \to 1$$
$$J_0(-kY_k) \to 1,$$
$$J_1(-kY_j) \approx -kY_i << 1,$$
$$i\left(J_0(-kY_j) - (-kY_j)^2/2\right)\cos(\theta_j) \approx i\cos(\theta_j).$$

As a result, Eq. (A.5) becomes

$$\frac{\partial g_j^*}{\partial y_i} g_k^* g_l^*(\vec{y},\vec{x},\omega) = -ik\frac{\partial Y_j}{\partial y_i}\frac{x_j}{x}, \tag{A.6}$$

which is in agreement with the low frequency assymptotic expression for the Green function proposed by Howe [9], [6].

B. Derivation of spanwise length

The integration along the span of the airfoil can be exressed as

$$\mathcal{L}_3(k, L_3) = \int_{-\infty}^{\infty} J_0(-ky_3)\exp\left(-\frac{y_3^2}{L_3^2}\right)dy_3 = 2\int_0^{\infty} J_0(-ky_3)\exp\left(-\frac{y_3^2}{L_3^2}\right)dy_3, \tag{B.1}$$

A closed form analytical expression is obtained for $\mathcal{L}_3$ by using the formula [19]

$$\int_0^{\infty} x^{\mu} e^{-\alpha x^2} J_n(\beta x)\,dx = \frac{\Gamma\left(\frac{1}{2}\nu + \frac{1}{2}\mu + \frac{1}{2}\right)}{\beta\alpha^{\mu/2}\Gamma(\nu+1)}\exp\left(-\frac{\beta^2}{8\alpha}\right)M_{\frac{1}{2}\mu,\frac{1}{2}\nu}\left(\frac{\beta^2}{4\alpha}\right), \Re[\alpha] > 0, \Re[\mu+\nu] > -1,$$

where $\Gamma(\cdot)$ the gamma function and $M_{\frac{1}{2}\mu,\frac{1}{2}\nu}(\cdot)$ the Whittaker function. By substituting $\mu = \nu = 0$, $\beta = -k$ and $\alpha = 1/L_3^2$ Eq.(B.2) becomes

$$\mathcal{L}_3(k, L_3) = -2\frac{\sqrt{\pi}}{k}\exp\left(-\frac{k^2L_3^2}{8}\right)M_{0,0}\left(\frac{k^2L_3^2}{4}\right). \tag{B.2}$$

Thus, the far-field pressure can be expressed as

$$p = \frac{-2U^2}{d}\mathcal{L}_3(k, L_3)\iint_{-\infty}^{\infty} A\exp\left(-\frac{(y_1/c + a)^2}{L_1^2}\right)\left(1 - \mathrm{erf}\left(\frac{y_1/c}{L_2}\right)\right)e^{i(k_1y_1+k_2y_2)}\mathcal{J}dy_1dy_2. \tag{B.3}$$